Impact of Ocean–Atmosphere Current Feedback on Ocean Mesoscale Activity: Regional Variations and Sensitivity to Model Resolution

SWEN JULLIEN,[a] SÉBASTIEN MASSON,[b] VÉRA OERDER,[c] GUILLAUME SAMSON,[d] FRANÇOIS COLAS,[b] AND LIONEL RENAULT[e,f]

[a] *Ifremer, Univ. Brest, CNRS, IRD, Laboratoire d'Oceanographie Physique et Spatiale, IUEM, Brest, France*
[b] *LOCEAN-IPSL, Sorbonne Université-CNRS-IRD-MNHN, Paris, France*
[c] *Escuela de Ciencias del Mar, Pontificia Universidad Católica de Valparaíso, Valparaiso, and Instituto Milenio de Oceanografía, Concepción, Chile*
[d] *Mercator Ocean, Ramonville-Saint-Agne, France*
[e] *University of Toulouse, IRD, CNRS, CNES, UPS, LEGOS, Toulouse, France*
[f] *Atmospheric and Oceanic Sciences, University of California, Los Angeles, Los Angeles, California*

(Manuscript received 3 July 2019, in final form 5 November 2019)

ABSTRACT

Ocean mesoscale eddies are characterized by rotating-like and meandering currents that imprint the low-level atmosphere. Such a current feedback (CFB) has been shown to induce a sink of energy from the ocean to the atmosphere, and consequently to damp the eddy kinetic energy (EKE), with an apparent regional disparity. In a context of increasing model resolution, the importance of this feedback and its dependence on oceanic and atmospheric model resolution arise. Using a hierarchy of quasi-global coupled models with spatial resolutions varying from 1/4° to 1/12°, the present study shows that the CFB induces a negative wind work at scales ranging from 100 to 1000 km, and a subsequent damping of the mesoscale activity by ~30% on average, independently of the model resolution. Regional variations of this damping range from ~20% in very rich eddying regions to ~40% in poor eddying regions. This regional modulation is associated with a different balance between the sink of energy by eddy wind work and the source of EKE by ocean intrinsic instabilities. The efficiency of the CFB is also shown to be a function of the surface wind magnitude: the larger the wind, the larger the sink of energy. The CFB impact is thus related to both wind and EKE. Its correct representation requires both an ocean model that resolves the mesoscale field adequately and an atmospheric model resolution that matches the ocean effective resolution and allows a realistic representation of wind patterns. These results are crucial for including adequately mesoscale ocean–atmosphere interactions in coupled general circulation models and have strong implications in climate research.

1. Introduction

The ocean is a highly turbulent environment characterized by a variety of structures ranging from basin-scale circulation to microscale turbulence, and by marked regional specificities (e.g., strong western boundary currents and eastern boundary upwelling systems). The total ocean kinetic energy (KE) has been shown to be dominated by the mesoscale geostrophic eddy field (Ferrari and Wunsch 2009). These mesoscale structures of $O(100)$ km are major players of the ocean circulation and transport of heat, salt, and biogeochemical tracers (e.g., Colas et al. 2012; Nagai et al. 2015; Dong et al. 2014). They are generated by the destabilization of the mean flow and can be dissipated toward smaller scales, feed back into the mean circulation (Ferrari and Wunsch 2009), or interact with the atmosphere.

A breakthrough in ocean modeling was made when increased resolution finally allowed us to resolve explicitly these mesoscale features (Smith et al. 2000; Maltrud and McClean 2005; Chassignet and Marshall 2008; McWilliams 2008). Long-living biases in global circulation models regarding western boundary currents separation, geographical extent of the gyres, or eddy kinetic energy (EKE) level have been consequently reduced. In addition to its direct impact on the ocean circulation, the eddy field has been shown to impact the atmosphere (Small et al. 2008, and references therein).

Supplemental information related to this paper is available at the Journals Online website: https://doi.org/10.1175/JCLI-D-19-0484.s1.

Corresponding author: Swen Jullien, swen.jullien@ifremer.fr

DOI: 10.1175/JCLI-D-19-0484.1

Indeed, at mesoscale, surface heat flux anomalies are created above the eddies (e.g., Bourras et al. 2004; Villas Bôas et al. 2015), and a coherent stress/wind response to sea surface temperature and surface current mesoscale structures has been observed (e.g., Chelton et al. 2001; Chelton and Xie 2010; O'Neill et al. 2010, 2012; Oerder et al. 2016; Renault et al. 2017a). The wind stress is affected by surface currents because it depends on the relative motion between the atmosphere and the ocean (i.e., on the "relative wind," which is the difference between absolute wind and surface current). Because surface currents are, in general, much weaker than winds (except in the equatorial band; e.g., Kelly et al. 2001), the use of a wind relative to the oceanic current [i.e., including the current feedback (CFB)] instead of an absolute wind when estimating the surface stress leads to small changes in the global wind stress and heat fluxes (1%–7%; Dawe and Thompson 2006; Duhaut and Straub 2006). Yet, it induces a large reduction of the wind power input to the ocean [the wind work (WWK)] evaluated between 15% and 35% (Duhaut and Straub 2006; Dawe and Thompson 2006; Hughes and Wilson 2008; Xu and Scott 2008; Scott and Xu 2009; Renault et al. 2016b). Indeed, the CFB always decreases the WWK (e.g., Oerder et al. 2018) whenever the currents and winds are in the same direction (WWK is then positive and reduced by current feedback) or opposed direction (WWK is then negative and becomes more negative). Two main impacts of the CFB are therefore noticeable: 1) at the large scale, the reduction of the mean WWK causes a slowing down of the oceanic circulation (Pacanowski 1987; Luo et al. 2005; Duhaut and Straub 2006; Hogg et al. 2009; Renault et al. 2016b, 2017b) and 2) at the mesoscale, rotating currents generate a wind stress curl opposed to the current vorticity (Rooth and Xie 1992; Renault et al. 2016a), inducing sinks of energy from the ocean to the atmosphere and, thus, a negative WWK at eddy scale (the eddy WWK). These sinks of energy are responsible for *eddy killing*, that is, a damping of the eddy kinetic energy by 10%–50% depending on the region (Dewar and Flierl 1987; Duhaut and Straub 2006; Zhai and Greatbatch 2007; Eden and Dietze 2009; Renault et al. 2016a,b, 2017b, 2019a; Seo et al. 2016; Seo 2017; Oerder et al. 2018). So far, this regional sensitivity has not been explained.

The wide range of wind power input and EKE sensitivities to the CFB reported in previous studies may be associated with differences in the studied regions, and/or in the model frameworks (analytical evaluations, forced ocean models, coupled models, or model spatial resolutions). One open question in coupled modeling frameworks is the need or not of having the very same spatial resolution in both the atmospheric and oceanic components to correctly resolve air–sea interactions. Using the same spatial resolution in both models could appear as the best solution to have the most coherent coupling between the ocean and the atmosphere, but is computationally expensive, mainly because of the high computational cost of atmospheric models. One possibility is thus to coarsen the spatial resolution of the atmospheric model. However, it is not clear yet whether this strategy would lead to similar results as an approach based on an atmospheric and oceanic model with the same spatial resolution.

The objective of this study is thus twofold. On the one hand, it aims to evaluate the mesoscale CFB effect on the ocean energetics at a quasi-global scale and to better understand its regional variations. On the other hand, this study strives to assess the dependence of the CFB to the spatial resolution of both the oceanic and atmospheric models. For that purpose, a quasi-global (46°S–46°N) realistic coupled model is used. Several simulations are performed differing by their spatial resolution and the degree of coupling they consider (with or without CFB). The main set of experiments uses a 1/12° oceanic resolution and a 1/4° atmospheric resolution (see section 2b). Two additional pairs of coupled simulations are then carried out in which the oceanic or the atmospheric spatial resolution is altered (i.e., coarsened or increased). After describing the models and methods in section 2, section 3 assesses the damping of the mesoscale activity by the CFB and the underlying mechanisms. The dependence of the results on the model spatial resolution is then addressed in section 4. The results are finally discussed and summarized in section 5.

2. Models and methods

a. Models

The regional coupled model framework used in this study was built from the NEMO-OASIS-WRF (NOW; acronyms defined below) coupled architecture (Samson et al. 2014). The atmospheric component is the Weather Research and Forecasting (WRF) Model with the Advanced Research version of WRF (ARW) dynamic solver (Skamarock et al. 2008), in its 3.3.1 version. ARW was especially designed with high-order numerical schemes to enhance the model's effective resolution of mesoscale dynamics (Skamarock 2004). The oceanic component is the Nucleus for European Modeling of the Ocean (NEMO) in its version 3.4 (Madec 2008), and the coupler is OASIS3-MCT (Craig et al. 2017; OASIS stands for Ocean Atmosphere Sea Ice Soil). Details about the model's setup (grid, numerical, and physical parameterizations) are given below, and are very similar

to those described in Samson et al. (2017) and Renault et al. (2019a).

The atmospheric model uses 60 vertical eta levels. The WRF default vertical resolution has been multiplied by three below 800 hPa. Thus, the first 33 levels are located below 500 hPa with a vertical resolution of 2 hPa near the surface. The vertical resolution then decreases to ~50 hPa around 800 hPa, and increases again when approaching the top of the model (50 hPa) with ~6 hPa for the top level. The choice of WRF physical parameterizations relies on previous studies (Samson et al. 2014, 2017; Crétat et al. 2016), which demonstrate the ability of this model setup to faithfully reproduce the tropical climate mean state and modes of variability. This physical setup includes: the longwave Rapid Radiative Transfer Model (RRTM; Mlawer et al. 1997), the Goddard shortwave radiation scheme (Chou and Suarez 1999), the WSM6 microphysics scheme (Hong and Lim 2006), the Betts–Miller–Janjic (BMJ) convection scheme (Betts and Miller 1986; Janjić 1994), Yonsei University (YSU) planetary boundary layer scheme (Hong et al. 2006), and the unified Noah land surface model (LSM) with the surface layer scheme from MM5 (Chen and Dudhia 2001).

The ocean model has 75 vertical z levels with 25 levels above 100 m and a resolution ranging from 1 m at the surface to 200 m at the bottom. Partial filling of the deepest cells is allowed (Barnier et al. 2006). The numerical settings of the 1/12° ocean configuration consist of an upstream-biased third-order advection scheme (UBS; Shchepetkin and McWilliams 2009) for the tracers and the dynamics with no explicit diffusivity and viscosity. The 1/4° configuration uses an iso-neutral Laplacian for tracer lateral diffusion with a constant coefficient of $300\,m^2\,s^{-1}$, a total variance dissipation scheme (Lévy et al. 2001) for tracer advection, a horizontal bi-Laplacian for momentum lateral diffusion of $-1.8 \times 10^{11}\,m^4\,s^{-1}$, and a vector invariant formulation of momentum equations with an energy–enstrophy conserving scheme for the vorticity term. In all experiments, the vertical mixing is parameterized using an improved version of a turbulent kinetic energy closure scheme (Blanke and Delecluse 1993) including a Langmuir cell (Axell 2002) and a surface wave breaking (Mellor and Blumberg 2004) parameterizations. The Gent–McWilliams parameterization is not used in any of our configurations.

b. Configuration and experiments

The coupled model geographical domain is a tropical channel that extends from 46°S to 46°N and therefore excludes sea ice covered areas. The OASIS coupler (Craig et al. 2017) exchanges the time-averaged surface fields between the models every hour. The impact of the atmospheric forcing temporal resolution in ocean-forced models has also been shown to affect the wind power input to the ocean (e.g., Zhai et al. 2012; Rimac et al. 2013). In our coupled framework the coupling frequency of 1 h allows us to resolve near-inertial motions, and appears as a reasonable choice as the parameterization of air–sea fluxes relies on a bulk formula whose range of validity is on the order of 1 h–1 day.

The main set of experiments, control simulations (CTRL), has a spatial resolution of 1/12° in the ocean and 1/4° in the atmosphere. The coupled fields are interpolated by averaging 3 point × 3 point tiles (as the ocean grid is an exact subdivision of the atmospheric one) with an eventual weighted average if masked points are located in the tile. Two simulations are performed: one that includes both sea surface temperature (SST) and current feedbacks to the atmosphere (CTRL_CFB) and one that does not include the current feedback (CTRL_NOCFB). In CTRL_CFB, the SST and surface currents $\mathbf{U}_o$ (first level of the oceanic model) are sent to the atmospheric model; the surface stress is then computed using a relative wind to the ocean motion ($\mathbf{U}_r = \mathbf{U}_a - \mathbf{U}_o$, where $\mathbf{U}_a$ is the first-level wind located at ~10 m). To properly implement the CFB in coupled models and represent its effect on the mesoscale activity, both the bulk formula and the discretization of turbulent vertical mixing term have to be modified. The former ensures consideration of the effect on the stress norm, whereas the latter allows us to properly compute the wind stress orientation (Lemarié 2015; Renault et al. 2019d). In CTRL_NOCFB simulations, only the SST is sent from the ocean to the atmosphere with no modification of the surface wind and stress by CFB. In all the simulations, hourly averages of heat, freshwater, and momentum fluxes are sent from the atmosphere to the ocean model.

Atmosphere initial state and lateral boundary conditions, at the northern and southern boundaries over the 1989–93 period, are prescribed from the European Centre for Medium-Range Weather Forecasts ERA-Interim 3/4° resolution reanalysis (Dee et al. 2011). On the ocean side, the Drakkar 1/4° resolution global ocean model (Brodeau et al. 2010) is used as the lateral (northern and southern) boundary condition. The coupled model is started after a 5-yr spinup of the ocean model obtained from a 5-yr-long forced simulation starting from Drakkar 1/4° simulation in order to get a fully developed mesoscale activity at 1/12°. The atmospheric model adjusts in a few days and so does not require a specific spinup regarding the time scales we are interested in. The model is in a balanced energetic regime; the impact of coupling, and particularly CFB, is stabilized

TABLE 1. Summary of the six simulation characteristics in terms of grid resolution and ocean feedbacks.

Simulation name	Oceanic grid	Atmospheric grid	SST feedback	Current feedback
LOW_CFB	1/4°	1/4°	Yes	Yes
LOW_NOCFB	1/4°	1/4°	Yes	No
CTRL_CFB	1/12°	1/4°	Yes	Yes
CTRL_NOCFB	1/12°	1/4°	Yes	No
HIGH_CFB	1/12°	1/12°	Yes	Yes
HIGH_NOCFB	1/12°	1/12°	Yes	No

after ~3 months of simulation (see Fig. S1 in the online supplemental material).

To assess the sensitivity of the results to the spatial resolution of the atmosphere and of the ocean, two additional set of experiments are carried out:

- by degrading from CTRL the spatial resolution of the ocean to 1/4° (simulations called LOW_CFB and LOW_NOCFB) and
- by increasing from CTRL the spatial resolution of the atmosphere to 1/12° (simulations called HIGH_CFB and HIGH_NOCFB).

In these simulations, the resolution is the same in the atmosphere and ocean components, and the grid is shared by both models; coupled variables are thus exchanged directly without interpolation. Table 1 summarized the characteristics of each simulation.

c. *Satellite observational datasets*

The surface stress is obtained from the daily QuikSCAT gridded product from Ifremer (Bentamy et al. 2013), which has a spatial resolution of 0.25°. The sea level anomaly (SLA) is computed from the 0.25° AVISO daily absolute dynamic topography (Ducet et al. 2000), which is constructed by means of an optimal interpolation in time and space from combined and intercalibrated altimeter missions (Le Traon et al. 1998). Both datasets are used over a 5-yr common period: 2002–06 (note that the results are insensitive to the chosen period).

d. *Filtering procedure for extracting "mesoscale anomalies"*

We use a spatial filter of ~250 km to extract mesoscale features. The choice of this filter is discussed in section 3d and in the discussion (section 5). Mesoscale anomalies of a field ϕ are then defined as $\phi' = \phi - [\phi]$, with $[\phi]$ the field ϕ smoothed by a low-pass Gaussian spatial filter with a standard deviation σ of 4 grid points on the 1/4° grid and 12 grid points on the 1/12° grid. The Gaussian weights of points located at a distance larger than 3σ are considered zero. The Gaussian filter is thus applied on a $(6\sigma + 1) \times (6\sigma + 1)$ window. This represents a 25×25 (73×73) point box at 1/4° (1/12°), which corresponds to ~670 km at the equator and ~475 km at 45°N as our grid is built on a Mercator projection. Land points are treated as missing data, and the weights of windows including land points are renormalized over the remaining oceanic points. The cutoff of this filter is between 240 and 330 km. To draw robust conclusions, the analyses of the present paper have also been reproduced using a 90-day temporal filter to extract mesoscale fields. For this purpose, the figures computed with the spatial filter (Figs. 1, 2, and 4) are compared to Figs. S2–S4 computed with the temporal filter (see the supplemental material and section 5).

A spatiotemporal filter is also used to isolate solely the wind stress response to the mesoscale CFB, and to compare it to analytical estimations (in Fig. 6). First a temporal average (using a 29-day running mean) is performed to suppress the weather-related variability (Chelton et al. 2007a), and then the large-scale signal is removed using the high-pass Gaussian spatial filter described above.

e. *Mesoscale activity and eddy wind work*

The geostrophic eddy kinetic energy (EKE), as a measure of the mesoscale activity, is evaluated in AVISO satellite altimetry product, and in the model, from sea level anomalies (SLA) as

$$\mathrm{EKE} = \frac{1}{2}(u_o'^2 + v_o'^2), \tag{1}$$

with (u_o, v_o) being the geostrophic current defined as $u_o = -(g/f)(\partial \mathrm{SLA}/\partial y)$ and $v_o = (g/f)(\partial \mathrm{SLA}/\partial x)$, and primes representing the mesoscale anomalies (see previous section); g is the gravitational acceleration and f the Coriolis parameter.

Note that in our study we consider only geostrophic ocean motions. Mesoscale currents, the topic to which this paper is dedicated, are indeed mostly geostrophic as the magnitude of the mesoscale ageostrophic motions is several orders lower than geostrophic mesoscale motions (Sasaki et al. 2014). Recent studies indicate a likely strong powering from submesoscale ageostrophic currents to mesoscale currents (Sasaki et al. 2014; Klein et al. 2019); however, our model setup is not built to study these submesoscale processes, as the resolution is

not fine enough and the coupling interface does not include waves, which could play a significant role in air–sea coupling at fine scales [$O(1)$ km] (e.g., Suzuki et al. 2014, 2016).

The input of energy by the wind to the ocean circulation, or wind work (WWK), is defined as the scalar product between wind stress $\boldsymbol{\tau}$ and ocean current $\mathbf{U}_o$ (with bold letters representing vectors):

$$\mathrm{WWK} = \boldsymbol{\tau} \cdot \mathbf{U}_o. \tag{2}$$

The eddy wind work (EWWK) in our simulations is the wind work associated with mesoscale anomaly fields, denoted by the prime, with mesoscale anomalies defined as detailed in section 2d using a spatial filter (or temporal for supplemental figures):

$$\mathrm{EWWK} = \boldsymbol{\tau}' \cdot \mathbf{U}_o'. \tag{3}$$

In the present study, we focus on the impact of CFB on EKE, and therefore EWWK. The mean WWK has already been shown to be decreased by CFB causing a slowdown of the oceanic circulation (Pacanowski 1987; Luo et al. 2005; Duhaut and Straub 2006; Hogg et al. 2009; Renault et al. 2016b, 2017b). Cross-terms, which are $[\boldsymbol{\tau}] \cdot \mathbf{U}_o'$ and $\boldsymbol{\tau}' \cdot [\mathbf{U}_o]$ (with square brackets denoting the large-scale fields and primes the mesoscale fields), are equal to 0 in a true Reynolds decomposition based on a temporal filtering (as performed in our supplemental information). In our WWK decomposition on large and eddy scales based on a spatial filter, the Reynolds decomposition is not valid and the 5-yr mean of the two cross-terms is therefore not exactly equal to 0 but has a negligible contribution compared with EWWK (not shown).

3. Damping of the mesoscale activity by the CFB

a. Evaluation of the EKE

The geostrophic EKE is first evaluated from AVISO and CTRL_CFB (see section 2e). Consistent with the literature (e.g., Ducet et al. 2000), the spatial distribution of the EKE is characterized by a strong disparity of energy levels, which are distributed over three orders of magnitude (delimited by the black contours in Fig. 1a). Very rich eddying regions are composed of western boundary currents (WBCs; the Gulf Stream, Kuroshio, Eastern Australian Current, Agulhas Current, Brazil Current, and Malvinas Current). They are characterized by strong mean currents that destabilize into eddies. Moderate eddying regions can be identified in the vicinity of WBCs, in the tropical Indian Ocean and western Pacific (where latitudinal jets instabilities generate mesoscale eddy structures, e.g., Couvelard et al. 2008), and in eastern boundary upwelling systems where EKE is relatively strong with respect to the mean kinetic energy. Finally, poor eddying regions are found in the center of the basins' gyres. The domain-mean EKE of the CTRL_CFB simulation has a general good agreement with respect to the observations ($\sim 0.015\,\mathrm{m^2\,s^{-2}}$ on average over the whole domain; Fig. 2, blue and black bars). The spatial patterns are also in agreement (not shown), even if the side panel of Fig. 1a reveals a bias compensation with positive biases at midlatitudes (associated with WBCs) and negative biases in the tropical bands (associated with the low energetic areas in the center of the basins). The model is underestimating the EKE intensity in the middle of the gyres because of its insufficient horizontal resolution to resolve the submesoscale dynamics that sustains mesoscale activity in these areas (Lévy et al. 2010; Sasaki et al. 2014). However, the optimal interpolation performed in the AVISO product also results in a smoothing and an underestimation of the EKE (Chelton et al. 2007b, 2011), contributing to the model–observation mismatch.

b. Characterizing the damping of EKE by the CFB

Figure 1b depicts the spatial distribution of the EKE difference between CTRL_CFB and CTRL_NOCFB as well as the latitudinal variations of its zonal average. The EKE reduction is characterized by a large spatial variability, and is negative everywhere with a few exceptions of positive spots in the vicinity of WBCs. These are caused by shifts of the mean currents' paths, which are associated with an increased stabilization of the WBCs induced by the CFB (Renault et al. 2016b, 2017b, 2019b). In average, the CFB causes a large damping of the EKE by 30%, and ignoring it leads to unrealistic EKE levels in CTRL_NOCFB (Fig. 2), consistently with previous studies (e.g., Renault et al. 2016a,b, 2017a; Seo et al. 2016; Seo 2017; Oerder et al. 2018).

To determine what drives the regional variations, three kinds of eddying regions are defined (see black contours in Fig. 1a): rich eddying regions ($\mathrm{EKE} > 0.1\,\mathrm{m^2\,s^{-2}}$), moderate eddying regions ($0.01\,\mathrm{m^2\,s^{-2}} < \mathrm{EKE} < 0.1\,\mathrm{m^2\,s^{-2}}$), and poor eddying regions ($\mathrm{EKE} < 0.01\,\mathrm{m^2\,s^{-2}}$). Blue bars in Fig. 3a illustrate the eddy-killing effect in each of these three types of regions for the CTRL simulations. The larger the EKE, the larger its absolute reduction, but the weaker its relative reduction: −22%, −34%, and −42% for high, medium, and low energetic regions, respectively. This result underlines the fact that the EKE reduction induced by the CFB is sensitive to the regional characteristics of the ocean dynamics. The next sections explain the spatial variations of the EKE reduction.

The ocean EKE can be modulated by two processes (other than advection and diffusion): 1) destabilization of the mean currents associated with shear (barotropic)

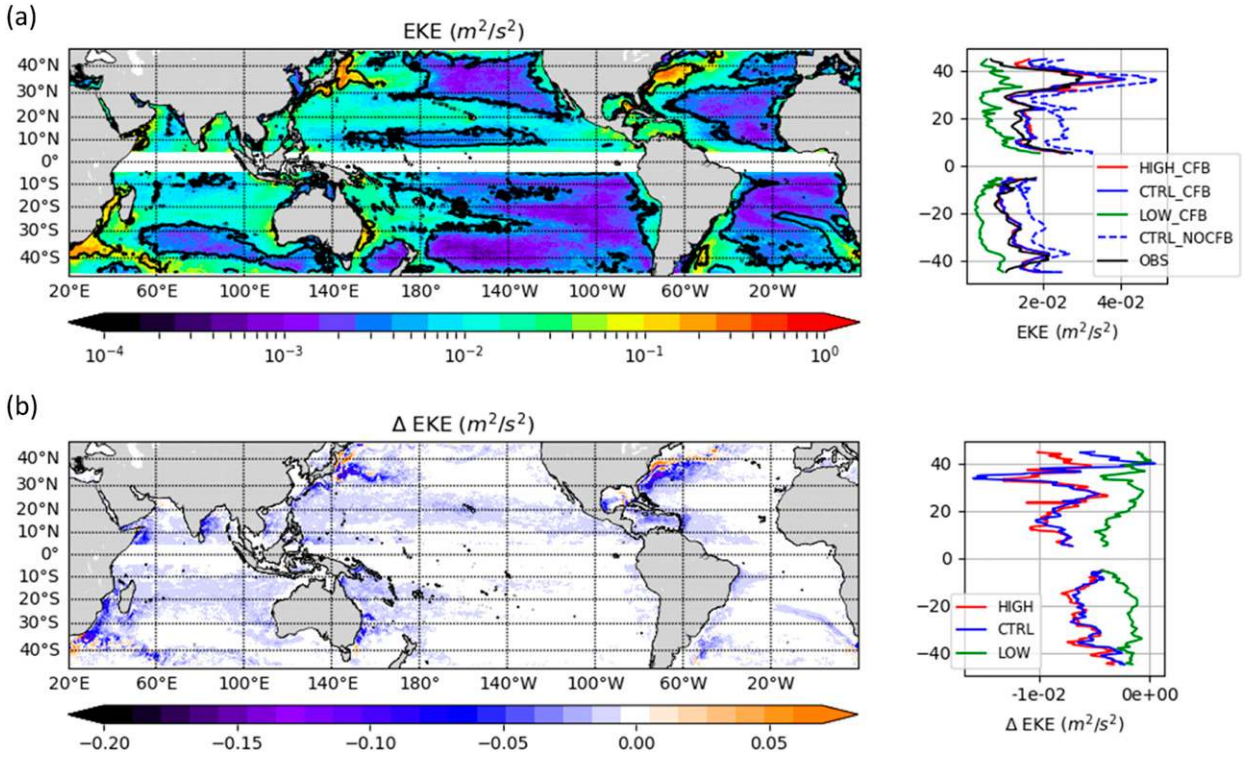

FIG. 1. (a) The 5-yr averaged geostrophic oceanic eddy kinetic energy (EKE) in the CTRL_CFB simulation and (b) difference between the CTRL_CFB and CTRL_NOCFB simulations. Side plots are zonal means of the corresponding map for HIGH (red), CTRL (blue), and LOW (green) simulations, and observations (black). The black contours in (a) separate regions of high (>0.1 $m^2\,s^{-2}$), medium (0.1–0.1 $m^2\,s^{-2}$), and low (<0.01 $m^2\,s^{-2}$) EKE.

or baroclinic instabilities and 2) exchange of energy between the ocean and the atmosphere by EWWK. In sections 3c and 3d, we evaluate the latter. To understand how the EWWK (and thus the EKE) is modified by the CFB, we first consider a simplified analytical framework (section 3c). To evaluate the impact of the simplifications introduced in section 3c, we then compare, in section 3d, the results obtained using this framework to those obtained through the actual introduction of the CFB in the simulations.

c. *Analytical development of the CFB*

Previous analytical studies (Bye 1985; Rooth and Xie 1992; Duhaut and Straub 2006; Gaube et al. 2015; Renault et al. 2017a) investigated the effect of the CFB on the EWWK by estimating the wind stress response to an ocean surface current perturbation $\mathbf{U}_o'$ as the difference between wind stress computed from absolute wind speed $\mathbf{U}_a$ and relative wind speed to the oceanic current $\mathbf{U}_r = \mathbf{U}_a - \mathbf{U}_o'$ (see also appendix):

$$\boldsymbol{\tau}'_{\text{diff}} = \rho_a C_d(|\mathbf{U}_r|\,\mathbf{U}_r - |\mathbf{U}_a|\,\mathbf{U}_a), \tag{4}$$

with the air density ρ_a and the drag coefficient C_d taken as constant values.

The EWWK associated with this estimation of wind stress response $\boldsymbol{\tau}'_{\text{diff}}$ to surface current perturbation $\mathbf{U}_o'$ is then estimated as

$$\text{EWWK}_{\text{diff}} = \boldsymbol{\tau}'_{\text{diff}} \cdot \mathbf{U}_o'. \tag{5}$$

Considering the three following approximations: $|\mathbf{U}_a| \gg |\mathbf{U}_o'|$, a small angle between $\mathbf{U}_o'$ and $\boldsymbol{\tau}'_{\text{diff}}$, and a randomly distributed angle between $\mathbf{U}_a$ and $\mathbf{U}_o'$, $\boldsymbol{\tau}'_{\text{diff}}$ can be approximated [see also Eq. (17) of Gaube et al. (2015), and the appendix] as follows:

$$\boldsymbol{\tau}'_{\text{diff}} \approx -\frac{3}{2}\rho_a C_d |\mathbf{U}_a|\,\mathbf{U}_o'. \tag{6}$$

We can here introduce an "analytical coupling coefficient" that can be interpreted as a measure of the intensity of the coupling between mesoscale currents and its wind stress response, and is therefore defined as

$$\boldsymbol{\tau}'_{\text{diff}} \approx s_{\tau\text{ana}}\,\mathbf{U}_o', \tag{7}$$

and is equal, according to Eq. (6), to

$$s_{\tau\text{ana}} = -\frac{3}{2}\rho_a C_d |\mathbf{U}_a|. \tag{8}$$

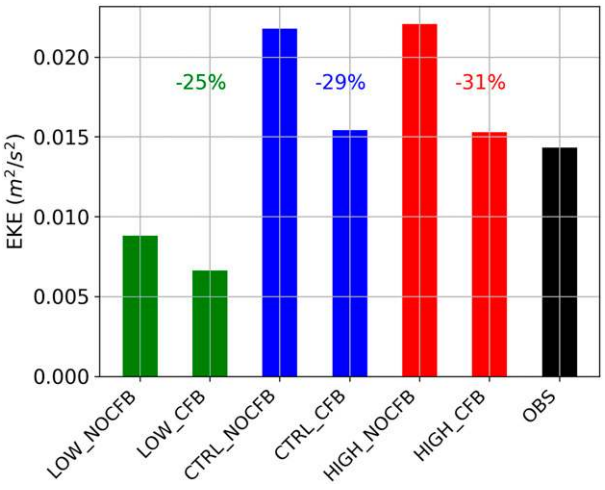

FIG. 2. The 5-yr geostrophic oceanic EKE averaged over the whole simulation domain for all simulations and the observations. Percentages indicate the difference between CFB and NOCFB for each set of simulations.

Using Eqs. (7) and (5) $\mathrm{EWWK}_{\mathrm{diff}}$ becomes

$$\mathrm{EWWK}_{\mathrm{diff}} \approx s_{\tau\mathrm{ana}} \mathbf{U}'_o \cdot \mathbf{U}'_o \approx 2 s_{\tau\mathrm{ana}} \mathrm{EKE}. \qquad (9)$$

In this analytical development, the analytical coupling coefficient $s_{\tau\mathrm{ana}}$ is thus always negative [Eq. (8)], and so is $\mathrm{EWWK}_{\mathrm{diff}}$ [Eq. (9)]. The CFB is thus supposed to induce a sink of energy from the ocean to the atmosphere which is proportional to the EKE.

Under the assumption that the CFB-induced EKE modifications (ΔEKE) are explained by the EWWK modifications (i.e., $\mathrm{EWWK}_{\mathrm{diff}}$), without considering processes associated with barotropic and baroclinic instabilities, then according to Eq. (9) the relative modification of EKE (ΔEKE/EKE in %) should be proportional to $s_{\tau\mathrm{ana}}$. This coefficient $s_{\tau\mathrm{ana}}$ only depends on the module of the absolute wind speed $|\mathbf{U}_a|$, which is mostly governed by the large-scale wind as most of wind energy is located at large scales (Fig. 7a). This linear dependency of $s_{\tau\mathrm{ana}}$ with $|\mathbf{U}_a|$ should thus explain the regional sensitivity of the relative EKE reduction. However, comparing Figs. 3a–c, we show that the regional variability of the relative reduction of EKE (ΔEKE/EKE in %) by the CFB is mainly constrained by EKE intensity (Fig. 3a). The proportionality to the wind magnitude $|\mathbf{U}_a|$ (Fig. 3b) is not visible, which is in contradiction with the analytical development aforementioned. Two main reasons can explain this apparent discrepancy. On one hand, the approximations made in the analytical development may be too crude. On the other hand, other oceanic processes may interfere with the EWWK action. These hypotheses are investigated in the following.

d. *Impact of the CFB in the simulations*

An important limitation of the aforementioned analytical development lies in the fact that $\mathbf{U}_a$ and $\mathbf{U}'_o$ are assumed to be unchanged when computing the change in wind stress $\boldsymbol{\tau}'_{\mathrm{diff}}$ and $\mathrm{EWWK}_{\mathrm{diff}}$ associated with the CFB, while $\mathbf{U}_a$ and $\mathbf{U}'_o$ are actually modified by the CFB. With our set of experiments, we can evaluate both the total CFB effect including all feedbacks (CTRL_CFB), and the predicted CFB from the analytical development using the CTRL_NOCFB experiment, which does not include these feedbacks. We can therefore compute a ''predicted'' CFB following the analytical development using CTRL_NOCFB to compute $\boldsymbol{\tau}'_{\mathrm{diff}}$ [Eq. (4)], $\mathrm{EWWK}_{\mathrm{diff}}$ [Eq. (5)], and its estimation from Eq. (9), and then compare it to the actual modeled EWWK computed from CTRL_CFB using Eq. (3) ($\mathrm{EWWK} = \boldsymbol{\tau}' \cdot \mathbf{U}'_o$).

As our focus is on the CFB, $\boldsymbol{\tau}'$ must be the response of the wind stress to the surface current perturbation $\mathbf{U}'_o$, as in the analytical development. One key point here is thus to isolate, within all the wind stress perturbations, the part of the signal that corresponds to the response to $\mathbf{U}'_o$. The better this signal in $\boldsymbol{\tau}'$ can be isolated, the more accurate the estimation of EWWK associated with the CFB will be. The spatial filter as detailed in section 2d is giving the best results to extract the anomalies of wind stress $\boldsymbol{\tau}'$ associated with $\mathbf{U}'_o$, especially in comparison with a 90-day temporal filter often used to characterize the oceanic mesoscale, but less appropriate to the time scales of the atmospheric variability.

The resulting EWWK map in CTRL_CFB is illustrated in Fig. 4 and is consistent with observations and previous studies (e.g., Hughes and Wilson 2008; Xu and Scott 2008; Xu et al. 2016; Renault et al. 2017a): EWWK is negative everywhere with more negative values over the rich eddying regions, revealing a large sink of energy from the mesoscale oceanic currents to the atmosphere. Note that EWWK estimated with a temporal filter shows similar patterns (Fig. S4) but with a much weaker signal-to-noise ratio (see discussion section). In CTRL_NOCFB, EWWK computed with Eq. (3) is almost null (side panel of Fig. 4b; see also Fig. S5), underlying the critical effect of the CFB on the EWWK, and indicating that the mesoscale thermal (SST) feedback has a very limited direct impact on the EWWK. The latter has also been confirmed in Renault et al. (2019a) by comparing a fully coupled experiment and an experiment including CFB but in which the SST is smoothed to keep only large-scale SST forcing but no mesoscale SST feedback to the atmosphere. Their two experiments reveal a similar behavior regarding the EWWK.

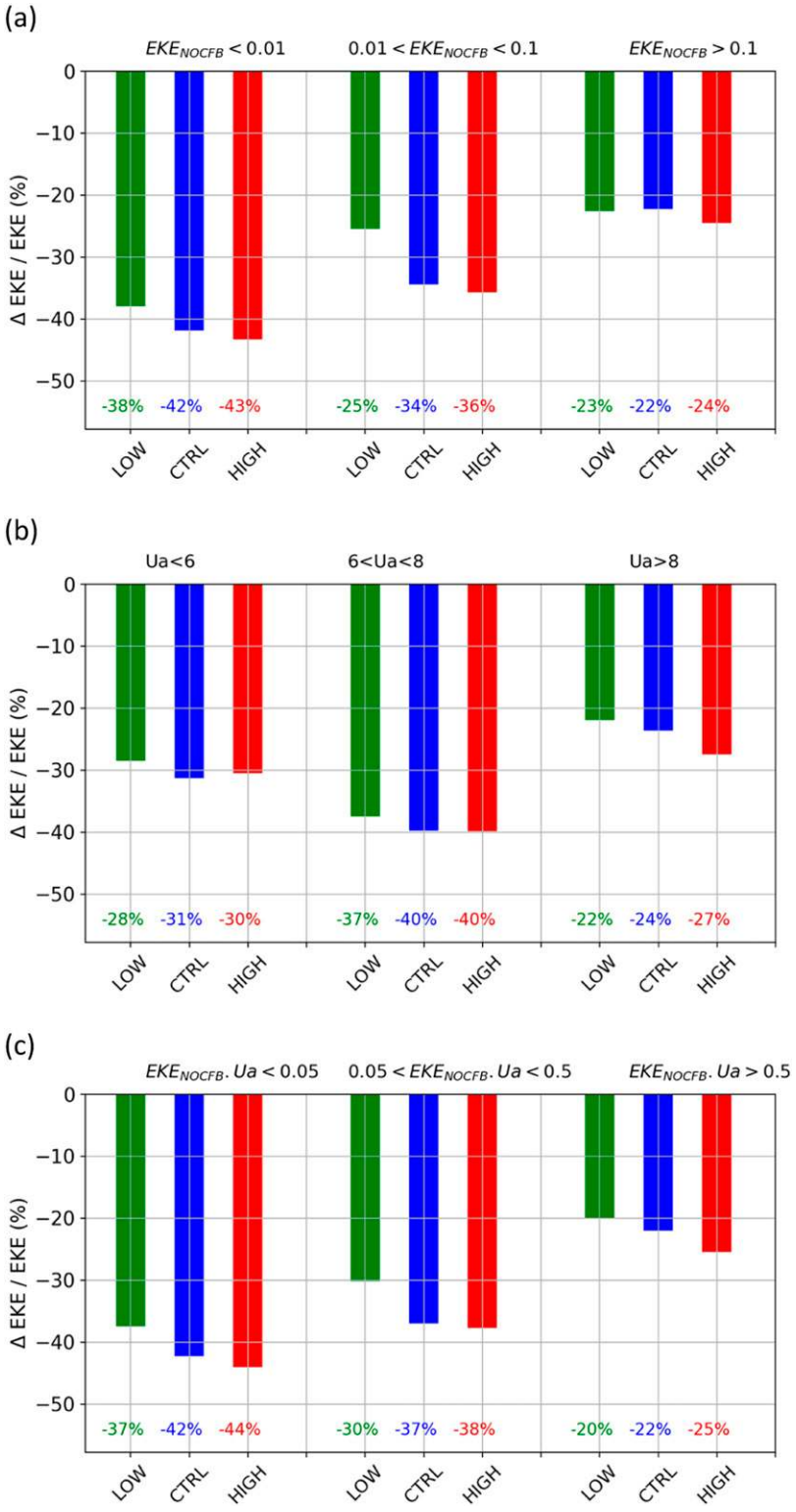

FIG. 3. Percentage of EKE decrease due to current feedback averaged over regions characterized by (a) their EKE level ($m^2 s^{-2}$) in NOCFB simulations (delimited by the black contours in Fig. 1a), (b) their wind speed U_a ($m s^{-1}$), and (c) a combination of wind speed and EKE ($m^3 s^{-3}$).

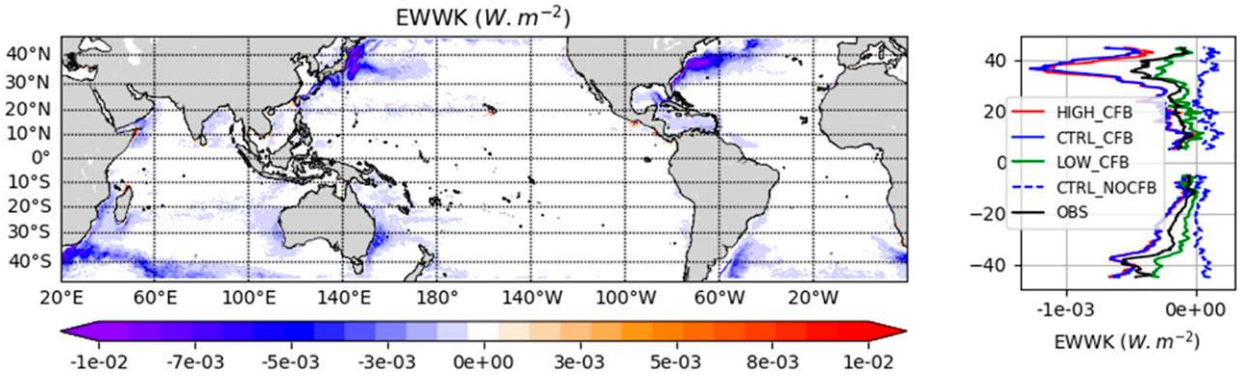

FIG. 4. The 5-yr average of eddy wind work (EWWK; W m^{-2}) in the CTRL_CFB simulation. The side plot represents the EWWK zonal average for HIGH_CFB (red), CTRL_CFB (blue), LOW_CFB (green), and CTRL_NOCFB (dashed blue) simulations, and observations (black).

The comparison of the analytically predicted CFB ($EWWK_{diff}$) computed from CTRL_NOCFB and the actual EWWK in CTRL_CFB is performed in Fig. 5a. Both estimations are highly correlated (0.87), and indicate that, as suggested by the analytical development, the CFB does induce a negative EWWK. This also confirms that the filtering procedure used to extract the mesoscale CFB signal in $\boldsymbol{\tau}'$ is able to isolate the wind stress response to mesoscale current. The EWWK estimated from CTRL_CFB is however weaker by ~30% with respect to $EWWK_{diff}$ (Fig. 5a; slope of the regression is 0.7). This may be due to the good but still imperfect filtering method, and to the approximations and limitations of the analytical approach (mainly the absence of CFB on $\mathbf{U}_a$ and $\mathbf{U}'_o$).

Figure 5b depicts the linear regression between EWWK (or $EWWK_{diff}$) and the reduction of EKE to asses to which extent the reduction of EKE between CTRL_CFB and CTRL_NOCFB (see section 3b and Figs. 1 and 2) can be related to the negative EWWK. EWWK and EKE reduction are significantly correlated (0.56; significant at 95%), supporting that the EWWK is the main driver of the weakening of mesoscale activity in CTRL_CFB, which is also suggested by the similarity between maps on Figs. 1b and 4. However, the correlation (0.56) is lower than in Fig. 5a, and the reduction of EKE is less and less sensitive to EWWK as the amplitude of EWWK increases, suggesting that other processes than EWWK impact the EKE reduction. Indeed, the contribution of intrinsic ocean instabilities has to be accounted for; this will be discussed at the end of section 3.

Finally, as suggested by Eq. (9) and the regression from Fig. 5b, we can verify to what extent the reduction of EKE is linked to the level of EKE in CTRL_NOCFB (Fig. 5c). It reveals a high negative correlation (−0.79) with a slope of ~−0.3 for low and moderate EKE levels, which explains exactly the value of −30% obtained in Fig. 2a. For stronger EKE bins, the distribution in Fig. 5c shows a flattening of the EKE reduction relatively to the linear regression, which corresponds to the regional values of Fig. 3a. This could be associated to the variability of the coupling coefficient s_τ or to other processes at play in the fully coupled model but not accounted for in the analytical development. Both are investigated in the following section.

e. *Efficiency of the EWWK and regional variability of the CFB*

As for the EWWK, the estimation of the coupling coefficient s_τ between ocean mesoscale currents and the wind stress response in CTRL_CFB requires a careful treatment in order to get an estimation with as less as possible noise. To do so, following Renault et al. (2016a), s_τ is computed for ''slowly moving rotating features'' (i.e., nondivergent geostrophic eddies) in CTRL_CFB by using the linear regression between spatiotemporal anomalies (see section 2d) of current vorticity and wind stress curl:

$$\mathrm{curl}(\boldsymbol{\tau}') = s_\tau \mathrm{curl}(\mathbf{U}'_o). \tag{10}$$

Note that s_τ appears negative everywhere (Fig. 6) and exhibits a spatial variability mainly related to the background winds distribution [Fig. 6; black contours denote the 8 m s^{-1} (solid) and 6 m s^{-1} (dashed) average wind]. This is highlighted by the seasonal variation of both winds and s_τ in Figs. 6a and 6b. Figure 6c depicts the distribution of s_τ as a function of the wind magnitude. Consistent with the analytical development [Eq. (8)] and satellite observations (Renault et al. 2017a), s_τ and the wind speed are characterized by a strong linear dependency (correlation of 0.73 with 95% confidence): the larger the wind speed, the more negative the s_τ. The slope of -2.3×10^{-3} of this linear regression is

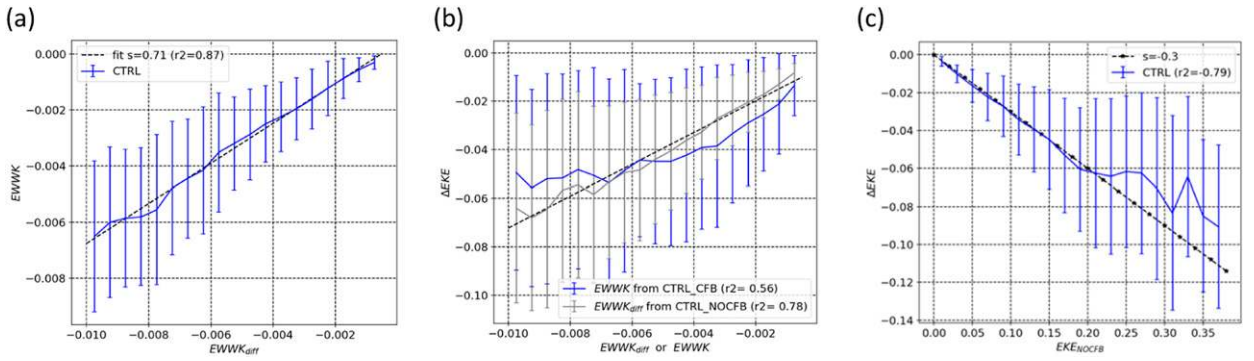

FIG. 5. (a) Regression between analytical eddy wind work difference due to the current feedback ($EWWK_{diff}$) computed from CTRL_NOCFB and the actual eddy wind work in CTRL_CFB (EWWK); (b) regression between EWWK (blue) or $EWWK_{diff}$ (gray), and the difference of EKE due to current feedback in CTRL ($\Delta EKE = EKE_{CTRL\_CFB} - EKE_{CTRL\_NOCFB}$); and (c) regression between EKE in CTRL_NOCFB and ΔEKE in CTRL. Dashed lines in (a) and (b) are the linear fits for CTRL_CFB. The star-dashed line in (c) is the linear regression with a slope equal to −0.3.

very close to the analytical value of -2.2×10^{-3} from Eq. (8) (with $C_d = 1.2 \times 10^{-3}$ and $\rho_a = 1.225\,\mathrm{kg\,m^{-3}}$) and to the observed value of -2.5×10^{-3} (Renault et al. 2017a). However, both in the observations and the model a positive offset exists, indicating a partial re-energization of the ocean (due to the full feedback loop: CFB induces a negative stress anomaly, which in turn causes a positive wind anomaly, which partially counteract the CFB nominal effect), which is not represented in the analytical development. Therefore s_τ can be predicted from $|\mathbf{U}_a|$ as $s_\tau = -2.3 \times 10^{-3}|\mathbf{U}_a| + 0.003$ ($\mathrm{N\,m^{-3}\,s^{-1}}$).

Assuming that the EWWK is the main driver of the EKE decrease and that s_τ represents its intensity, the relative reduction of EKE should depend only on the coupling coefficient, s_τ. The pattern of EKE reduction should be similar to that of s_τ and, thus, to $|\mathbf{U}_a|$ as s_τ can be also approximated as a linear expression of $|\mathbf{U}_a|$ [Eq. (8) and Fig. 6]. However, Fig. 1b and Fig. 3b do not support this assumption. Although the mean value of the EKE relative reduction (−30%; Fig. 2) is in agreement with the analytical estimate (Fig. 5c), its spatial pattern does not follow the analytical development (Figs. 1b and 3). Figure 5c confirms the broad view given in Fig. 3a: the CFB effect is less efficient in very rich eddying regions than in other regions while Eq. (9) suggests that CFB relative effect should be proportional to s_τ and therefore to $|\mathbf{U}_a|$ [Eq. (8)]. This apparent contradiction is explained by the fact that in rich and moderately rich eddying regions (e.g., WBCs and their surroundings) other processes than EWWK have a large influence on the EKE evolution. In these regions, consistent with Eq. (9) and Fig. 4, EWWK is stronger in amplitude than in other regions. However, the contribution of EWWK to EKE is balanced by barotropic and baroclinic instabilities (Zhai et al. 2010; Loveday et al. 2014) that are less affected by CFB [O(10%), Renault et al. 2017b]. By contrast, in poor eddying regions (e.g., the basin centers), baroclinic and barotropic instabilities are generally very weak (Zhai et al. 2010) and the EKE evolution is mainly controlled by EWWK. The relative impact of the CFB is therefore stronger (from ∼−30% to −40%).

To sum up, the relative impact of CFB is reduced in regions (WBCs) where EWWK is not the only driver of EKE, explaining the apparent link to the EKE level (Fig. 3a), and the weak effect of the spatial variations of s_τ and $|\mathbf{U}_a|$ (Figs. 3a–c).

4. Sensitivity to the model spatial resolution

The previous section evidenced the significant damping of the EKE by the CFB at the quasi-global scale as well as its regional sensitivity, which is associated with both the synoptic wind and the amplitude of the EKE itself. In the following, sensitivity of the results to the spatial resolution of both oceanic and atmospheric models is explored.

a. Sensitivity to the oceanic resolution

Not surprisingly, when diminishing the oceanic spatial resolution from 1/12° (CTRL_CFB) to 1/4° (LOW_CFB), the oceanic model becomes only eddy-permitting, except for the equatorial band [10°S–10°N; see also Fig. 1 from Hallberg (2013)]. EKE levels in LOW_CFB experiment are thus largely underestimated (3–10 times smaller than in CTRL_CFB; Fig. 1a side panel). However, despite these large EKE differences, the striking result when comparing LOW_NOCFB and LOW_CFB lies in the fact that the EKE damping (in %)

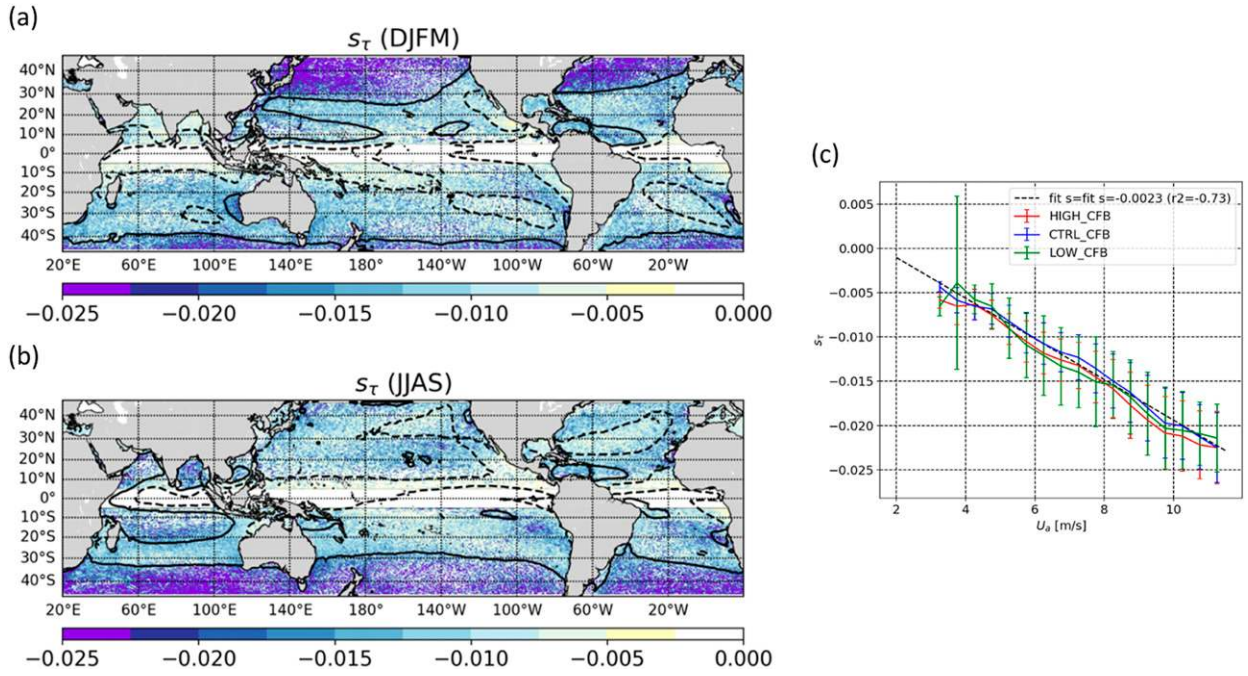

FIG. 6. Coupling coefficient s_τ, as defined by Eq. (10) in CTRL_CFB: (a) averaged over the five boreal winters [December–March (DJFM)] and (b) averaged over the five boreal summers [June–September (JJAS)]; black solid contours depict the 8 m s^{-1} wind speed, and black dashed contours depict the 6 m s^{-1} wind speed. Also shown is (c) s_τ averaged over the whole domain and seasons as a function of wind speed $\mathbf{U}_a$ in the three simulations HIGH_CFB (red), CTRL_CFB (blue), LOW_CFB (green). Points where the correlation coefficient is lower than 0.2 have been removed. The black dashed line is the linear fit for CTRL_CFB (with a slope of −0.023 and an offset of 0.003).

is very similar to that of CTRL experiments: −25%, compared to −29% (Fig. 2a). Additionally, the impact of the CFB is also characterized by the same regional variability (with a weaker impact in rich eddying regions, e.g., WBCs) from −38% to −23% (Fig. 3a). At the global scale, the relative reduction of EKE (in %) is almost insensitive to the oceanic spatial resolution, which is coherent with Eq. (9). Because the EKE is much weaker in the 1/4° than in the 1/12° ocean simulations, the impact of CFB is weaker in absolute value, but its relative contribution to the EKE level remains comparable regardless the resolution. The slightly weaker impact of CFB (in %) in LOW than in CTRL experiments can be explained by the CFB regional dependency. As explained in section 3e, in very rich eddying regions the EKE is controlled not only by the EWWK but also by baroclinic and barotropic instabilities. Because of its coarser spatial resolution, the EKE distribution in LOW_CFB is shifted toward WBCs regions in comparison with CTRL_CFB: low and medium bins of EKE (Fig. 3a) capture more points located in WBC regions in LOW_CFB than in CTRL_CFB. This explains why, for a given level of EKE, the relative influence of the EWWK is lower in LOW_CFB than in CTRL_CFB and, thus, why the relative impact of the CFB (in %) is weaker. In any case, it is worth noting that even with a relatively coarse model simulation $O(1/4°)$, CFB has still a strong impact on the mesoscale activity. Neglecting this process will artificially increase the insufficient EKE in such models, but for the wrong reasons (model errors compensation).

b. Sensitivity to the atmospheric resolution

By contrast, the increase of the atmospheric resolution from CTRL (1/4°) to HIGH (1/12°) has no significant impact either on the EKE levels (Fig. 2), or on the EKE reduction induced by the CFB. At first glance, this might be surprising. Atmospheric fine scales are better resolved in a 1/12° than in a 1/4° model. In addition, the coupling interface is more coherent in HIGH than in CTRL simulation, as in HIGH the ocean and atmosphere share the exact same grid, whereas in CTRL experiment, oceanic data are averaged over 3 point × 3 point boxes before being sent to the atmosphere. However, the insensitivity of the CFB to the atmospheric resolution in our experiments is explained by a combination of two facts. First, as demonstrated in section 3e, the coupling coefficient s_τ can be expressed as a function of wind magnitude $|\mathbf{U}_a|$ in agreement with the analytical results

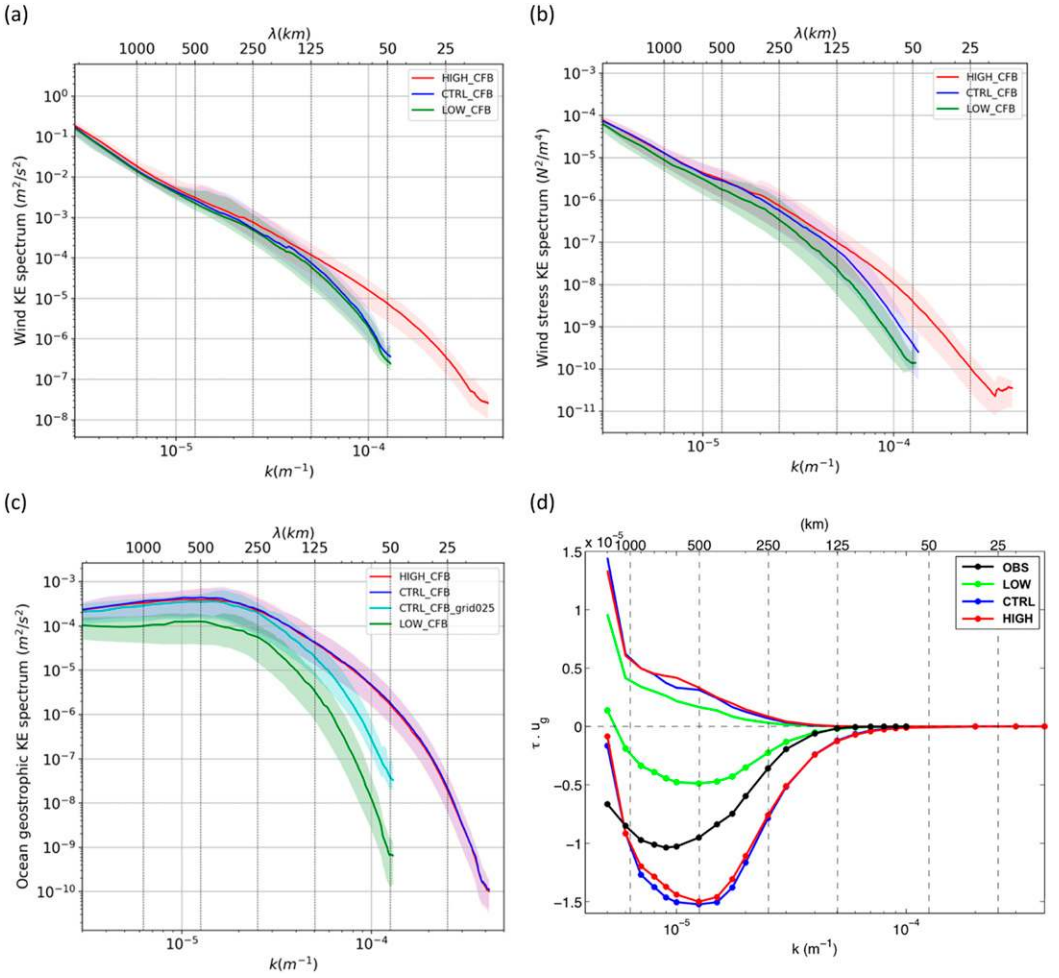

FIG. 7. (a) Wind speed power spectrum, (b) wind stress power spectrum, (c) geostrophic current power spectrum, and (d) cospectrum of the geostrophic wind work (WWKρ_0) as a function of wavenumber. All spectra are averaged over the whole oceanic domain, and over the 5 years of simulation, for the HIGH (red), CTRL (blue), and LOW (green) simulations. In (a)–(c) CFB simulations are represented. In (d) both CFB (star solid lines), and NOCFB (solid lines) are represented, as well as the observations (black). Note that in the spectral space, wavelengths are considered, and thus the minimal representable wavelength corresponds to two grid points.

of Eq. (8). As shown in Fig. 7a, most of the wind energy is located at large scales, and the differences between CTRL and HIGH winds are hardly visible at scales larger than 125–150 km. This explains why the coupling coefficient s_τ, which is proportional to $|\mathbf{U}_a|$, is consistently similar in all the simulations (Fig. 6). The intensity of the coupling between mesoscale surface currents and its wind stress response is thus insensitive to the differences in model resolutions considered in this study.

Second, the identical impact of CFB in HIGH and CTRL experiments is also explained by the effective and nominal spatial resolutions of the oceanic and atmospheric models, respectively. The distribution of wind work (WWK) among scales and regions is illustrated by the wind stress and surface current cospectrum (Fig. 7d). In the simulations that ignore CFB (NOCFB simulations), consistent with the absence of sinks of energy and eddy killing, the cospectrum is positive everywhere, indicating that energy is injected from the atmosphere to the ocean at any scale. In all the simulations with CFB (CFB simulations, solid lines with dots), the cospectrum is negative for scales ranging from ~100 to ~1000 km, reflecting the sink of energy from the ocean to the atmosphere. These scales mainly correspond to oceanic eddies, and extended meandering structures (Gulf Stream, Kuroshio, etc.). In a 1/12° oceanic simulation, the scales mostly affected by CFB are in a range fairly well represented by the atmospheric 1/4° resolution (Figs. 7a,d). Note that at larger scales, not represented in the

cospectrum, the atmosphere forces the ocean, which is reflected by a positive WWK (albeit weakened by the CFB: Pacanowski 1987; Luo et al. 2005; Duhaut and Straub 2006; Hogg et al. 2009; Renault et al. 2016b, 2017b).

The effective resolution of the 1/12° ocean model is about 6–7 times the grid spacing (~50–60 km; Soufflet et al. 2016), and the surface currents of the 1/12° ocean model sent to the 1/4° atmospheric model are not significantly affected by the 3 × 3 point box average. This is clearly visible on ocean kinetic energy spectrum (Fig. 7c) where the 1/12° current spectrum computed on the 1/12° (blue line) and on the 1/4° grid (cyan line) are identical for scales larger than 250 km, and very little affected for scales between 125 and 250 km. Therefore, scales affected by CFB (from ~100 to ~1000 km) are not impacted by the 3 × 3 point box average. Consequently, in order to ensure a proper representation of CFB, the atmospheric model grid must have a grid resolution fine enough to "see" and respond to the oceanic currents. The required atmospheric resolution is thus driven by the effective resolution of the ocean model in order to keep acceptable levels of oceanic EKE seen by the atmosphere.

These results explain why the CTRL simulation has an atmospheric resolution fine enough to correctly represent the CFB, and why using the HIGH resolution does not significantly alter neither the sinks of energy nor the EKE. The atmospheric nominal resolution should match the ocean effective resolution. Thus, an atmospheric resolution 3–5 times lower than that of the ocean is suitable if it remains fine enough to properly represent large-scale surface wind speed (>500 km), which controls the intensity of the coupling coefficient s_τ. Note that this atmospheric resolution constraint concerns only the representation of the CFB on a broad perspective. Other processes or local air–sea coupling effects, for example in coastal regions, may require a higher-resolution atmospheric grid to be correctly accounted for.

5. Discussion and conclusions

The current feedback (CFB) induces a negative eddy wind work (EWWK) that reveals a sink of energy from the mesoscale oceanic currents to the atmosphere. This sink of energy is responsible for a damping of the geostrophic mesoscale activity by roughly 30%. While the amplitude of the mesoscale activity reduction, and of the sink of energy are larger over rich eddying regions, paradoxically, the relative impact of CFB on the mesoscale activity is more efficient (up to 40%) over poor eddying areas. This counterintuitive result is explained by regional differences in the balance between ocean intrinsic instabilities and EWWK: in rich eddying regions, barotropic and baroclinic ocean instabilities are strong and thus the relative contribution of EWWK to the EKE is not as strong as in other regions. Consequently, the CFB relative contribution to the EKE reduction is less important in rich-eddying regions. This explains the wide range of EKE damping sensitivity to the CFB found in previous regional coupled studies (e.g., Renault et al. 2016a,b, 2017b; Seo et al. 2016; Seo 2017; Oerder et al. 2018). In agreement with these previous studies, we also find that the CFB impact on the vertically integrated (or barotropic) EKE is slightly lower but certainly not negligible (−16%), showing the same pattern and processes as geostrophic EKE (Fig. S7). Furthermore, we show that the amplitude of the negative EWWK caused by the CFB is driven by the level of EKE and by the coupling coefficient between mesoscale surface current and surface stress s_τ. The largest sinks of energy are located over rich eddying regions where s_τ is particularly negative. Consistent with previous results, we demonstrate that s_τ can be predicted as a function of wind speed magnitude (Bye 1985; Rooth and Xie 1992; Duhaut and Straub 2006; Gaube et al. 2015; Renault et al. 2017a). The analytical framework developed in previous studies (Rooth and Xie 1992; Duhaut and Straub 2006; Gaube et al. 2015), however, overestimates (by ~30%) the predicted EWWK due to the omission of $\mathbf{U}_a$ and $\mathbf{U}'_o$ changes due to the CFB (feedback loop).

The sensitivity to the model resolution is assessed by comparing the CTRL simulations (spatial resolution of 1/12° for the ocean, and 1/4° for the atmosphere) to two sets of simulations in which model resolution is degraded in the ocean from 1/12° to 1/4°(LOW) or increased in the atmosphere from 1/4° to 1/12° (HIGH). The main result is that regardless of the horizontal resolution in our set of simulations, the relative decrease of EKE from a simulation without CFB to a simulation with CFB is similar (from −25% to −30%). Not surprisingly, the 1/4° oceanic simulations have a much lower EKE than the 1/12° simulations, and, consistent with previous findings, the subsequent sink of energy is weaker. However, the relative decrease of EKE (in %) at low resolution (1/4°) remains quite similar to the one observed at higher resolution (1/12°). Ignoring the CFB at low resolution will thus artificially increase the too-low EKE in such models (errors compensation). More interestingly, we demonstrate that the eddy killing is insensitive to an increase in the atmospheric model spatial resolution from 1/4° to 1/12°. This result is explained by the combination of two factors. First, the coupling coefficient s_τ is proportional to the surface wind magnitude, and is therefore insensitive to model resolution as long as large-scale winds, which account

for most of the wind energy, are correctly represented. The simulations with a 1/12° ocean resolution and 1/4° or 1/12° atmosphere resolution have consequently a comparable s_τ, and subsequent sink of energy. Second, the correct representation of CFB requires the atmospheric nominal resolution to be finer than the oceanic effective resolution, which is the case in all our simulations. With similar spatial resolution, the computational cost of an ocean–atmosphere coupled model is mostly attributable to the atmospheric component. Our results allow us to answer a long-standing question about the necessity, or not, to have the same oceanic and atmospheric spatial resolution to correctly resolve mesoscale air–sea energy transfers, and their implications on ocean energetics. With such a focus, the required atmospheric resolution in a coupled model should be driven by the effective resolution of the ocean model. A factor of 3 (or even up to 5) between the spatial resolution of the oceanic model and that of the atmospheric model is therefore largely acceptable in terms of mesoscale air–sea coupling and exchange of energy between the ocean and the atmosphere. These results are obviously valid for the open ocean, and are not necessarily true for regions characterized by specific coastal effects that would need to be resolved by the atmospheric model. In addition, our study only addresses the impact of CFB on the wind input and ocean geostrophic EKE; it does not assess the impact of both CFB and SST feedback on the atmospheric boundary layer (more than wind stress; e.g., Putrasahan et al. 2013; Oerder et al. 2016), which may be differently sensitive to the atmospheric resolution (but keeping in mind that the SST gradients are affected by the effective resolution of the model as currents are). Recent studies (e.g., Su et al. 2018) have also suggested that submesoscale motions could significantly impact the air–sea exchanges and heat transport. Such effects may be accounted for in higher-resolution studies that resolve submesoscale, and their potential influence on the results of the present study should be assessed.

The extraction of the mesoscale anomalies appears sensitive to the filtering procedure mainly because of the different spatial and temporal scales that characterize oceanic and atmospheric circulations. We therefore reproduced all of our diagnostics using a temporal filter (a 90-day temporal filter, which is a typical temporal scale used to select oceanic mesoscale; see Figs. S2–S4). This temporal filter is less selective than the spatial filter especially for the atmospheric component as almost all the atmospheric energy is concentrated at scales smaller than 90 days. This filter is thus less appropriate to select the atmospheric response to the mesoscale coupling and, for example, the EWWK estimated using the temporal filter is therefore less consistent with the analytical development than the EWWK estimated using a spatial filter (see section 3d). While the main sinks of energy are still present (but noisy), the center of the gyres and the nearshore regions are characterized by a positive EWWK, which is due to the presence of wind-driven currents (see Fig. 4 and Fig. S4). These large differences could question our results and their robustness to the filtering procedure. The key point to answer this comment is that most of the differences related to the method chosen to define the mesoscale will mostly cancel each other as soon as we consider differences between simulations with and without CFB. For instance, the sink of energy defined as (EWWK_CFB − EWWK_NOCFB) is similar for both filters (see Fig. S6), and the EKE decrease from NOCFB to CFB experiments show similar amplitudes, and the same regional sensitivity with a spatial or a temporal filter (Fig. 2 and Fig. S2). The choice of using a spatial filter in this work has been driven by the willingness of getting a more accurate selection of the atmospheric response to the presence of mesoscale surface current in order to get results closer to the analytical framework.

To conclude, our results confirm the ubiquitous importance of the CFB on the ocean EKE distribution. This has a large implication for the ocean modeling community as it emphasizes the fact that the CFB should be taken into account also in forced ocean models (even at low resolution) in order to obtain a realistic representation of both the large-scale and mesoscale circulations. To achieve this, a promising perspective is to use a parameterization of the CFB based on the coupling coefficient s_τ (Renault et al. 2019c).

Finally, our results are very relevant for the climate modeling community as they provide guidance to determine the adequate atmospheric spatial resolution in coupled models. The atmospheric model is computationally the most expensive component, which generally prevents its resolution increase to ocean eddy-resolving nominal resolution. We show here that ocean–atmosphere interactions at the ocean mesoscale can be efficiently taken into account in coupled models without having to work with a computationally prohibitive atmospheric resolution.

Acknowledgments. This work was supported by the PULSATION ANR-11-MONU-010 project of the French National Research Agency (ANR). S.J. appreciated support from Ifremer, and L.R. from the National Science Foundation (OCE-1419450). We thank the GENCI-TGCC for the computing resources (Grants A0010106895, A0030106895, A0050106895).

APPENDIX

Analytical Development of the CFB

The analytical framework of CFB as summarized in section 3 is detailed here. It is based on the previous works by Bye (1985), Rooth and Xie (1992), Duhaut and Straub (2006), Gaube et al. (2015), and Renault et al. (2017a). This appendix details the step by step simplifications and assumptions made in this analytical framework. The effect of the CFB on the wind stress is assessed by computing a difference between wind stress computed from absolute wind speed $\mathbf{U}_a$ and relative wind speed to the oceanic current:

$$\boldsymbol{\tau}_{\text{diff}} = \underbrace{\rho_a C_d |\mathbf{U}_a - \mathbf{U}_o| (\mathbf{U}_a - \mathbf{U}_o)}_{\text{Relative wind stress}} - \underbrace{\rho_a C_d |\mathbf{U}_a| \mathbf{U}_a}_{\text{Absolute wind stress}}, \tag{A1}$$

with

$$|\mathbf{U}_a - \mathbf{U}_o| = \sqrt{|\mathbf{U}_a|^2 + |\mathbf{U}_o|^2 - 2\mathbf{U}_a \cdot \mathbf{U}_o} \quad \text{and} \tag{A2}$$

$$\mathbf{U}_a \cdot \mathbf{U}_o = |\mathbf{U}_a| \, |\mathbf{U}_o| \cos\theta. \tag{A3}$$

Considering that (first approximation)

$$|\mathbf{U}_a| \gg |\mathbf{U}_o|, \tag{A4}$$

Eq. (A2) becomes

$$\begin{aligned} |\mathbf{U}_a - \mathbf{U}_o| &\approx \sqrt{|\mathbf{U}_a|^2 - 2|\mathbf{U}_a| \, |\mathbf{U}_o| \cos\theta} \\ &\approx |\mathbf{U}_a| \sqrt{1 - 2\frac{|\mathbf{U}_o|}{|\mathbf{U}_a|} \cos\theta}, \end{aligned} \tag{A5}$$

and with

$$\sqrt{1-x} \approx 1 - \frac{x}{2}, \quad \text{if} \quad |x| = 1 \tag{A6}$$

Eq. (A5) becomes

$$\begin{aligned} |\mathbf{U}_a - \mathbf{U}_o| &\approx |\mathbf{U}_a| \left(1 - \frac{|\mathbf{U}_o|}{|\mathbf{U}_a|} \cos\theta\right), \\ &\approx |\mathbf{U}_a| - |\mathbf{U}_o| \cos\theta \end{aligned} \tag{A7}$$

and Eq. (A1) becomes

$$\begin{aligned} \boldsymbol{\tau}_{\text{diff}} &\approx \rho_a C_d [|\mathbf{U}_a| - |\mathbf{U}_o| \cos\theta (\mathbf{U}_a - \mathbf{U}_o) - |\mathbf{U}_a| \mathbf{U}_a] \\ &\approx -\rho_a C_d (|\mathbf{U}_a| \mathbf{U}_o + \mathbf{U}_a |\mathbf{U}_o| \cos\theta). \end{aligned} \tag{A8}$$

If we define $(\mathbf{i}, \mathbf{j})$ the unit vector (pointing in, perpendicular to) the direction of $\mathbf{U}_a$:

$$\mathbf{U}_a = |\mathbf{U}_a| \, \mathbf{i}, \tag{A9}$$

$$\mathbf{U}_o = |\mathbf{U}_o| \cos\theta \, \mathbf{i} + |\mathbf{U}_o| \sin\theta \, \mathbf{j}, \tag{A10}$$

Eq. (A8) becomes

$$\begin{aligned} \boldsymbol{\tau}_{\text{diff}} &\approx -\rho_a C_d (|\mathbf{U}_a| \, |\mathbf{U}_o| \cos\theta \, \mathbf{i} + |\mathbf{U}_a| \, |\mathbf{U}_o| \sin\theta \, \mathbf{j} \\ &\quad + |\mathbf{U}_a| \, |\mathbf{U}_o| \cos\theta \, \mathbf{i}) \\ &\approx -\rho_a C_d |\mathbf{U}_a| \, |\mathbf{U}_o| (2\cos\theta \mathbf{i} + \sin\theta \mathbf{j}). \end{aligned} \tag{A11}$$

We define

$$\mathbf{e} = \cos\theta \mathbf{i} + \frac{1}{2} \sin\theta \mathbf{j}, \tag{A12}$$

and its module:

$$\begin{aligned} |\mathbf{e}| &= \sqrt{\cos^2\theta + \frac{1}{4}\sin^2\theta} \\ &= \sqrt{\cos^2\theta + \frac{1}{4}(1 - \cos^2\theta)}, \quad \text{with} \quad \cos^2\theta + \sin^2\theta = 1 \\ &= \frac{1}{2}\sqrt{1 + 3\cos^2\theta}. \end{aligned} \tag{A13}$$

Making two approximations, which are verified at the mesoscale [see also the appendix of Renault et al. (2017a)], it is shown that

1) The angle between $\mathbf{U}_o$ and $\boldsymbol{\tau}'_{\text{diff}}$ is small

$$|\mathbf{U}_o| \cdot \mathbf{e} \approx \mathbf{U}_o \, |\mathbf{e}|; \quad \text{and} \tag{A14}$$

2) θ has a random and uniform distribution between 0 and 2π, and then $|\mathbf{e}|$ can be replaced by its mean value, which is ~3/4.

Then finally, the eddy-killing effect can be approximated to

$$\boldsymbol{\tau}'_{\text{diff}} \approx -\frac{3}{2} \rho_a C_d |\mathbf{U}_a| \, \mathbf{U}'_o. \tag{A15}$$

REFERENCES

Axell, L. B., 2002: Wind-driven internal waves and Langmuir circulations in a numerical ocean model of the southern Baltic Sea. *J. Geophys. Res.*, **107**, 3204, https://doi.org/10.1029/2001JC000922.

Barnier, B., and Coauthors, 2006: Impact of partial steps and momentum advection schemes in a global ocean circulation model at eddy-permitting resolution. *Ocean Dyn.*, **56**, 543–567, https://doi.org/10.1007/s10236-006-0082-1.

Bentamy, A., S. A. Grodsky, B. Chapron, and J. A. Carton, 2013: Compatibility of C- and Ku-band scatterometer winds: ERS-2 and QuikSCAT. *J. Mar. Syst.*, **117–118**, 72–80, https://doi.org/10.1016/j.jmarsys.2013.02.008.

Betts, A., and M. Miller, 1986: A new convective adjustment scheme. Part II: Single column tests using GATE wave, BOMEX, ATEX and Arctic air-mass data sets. *Quart. J. Roy. Meteor. Soc.*, **112**, 693–709, https://doi.org/10.1002/QJ.49711247308.

Blanke, B., and P. Delecluse, 1993: Variability of the tropical Atlantic Ocean simulated by a general circulation model with two different mixed-layer physics. *J. Phys. Oceanogr.*, **23**, 1363–1388, https://doi.org/10.1175/1520-0485(1993)023<1363:VOTTAO>2.0.CO;2.

Bourras, D., G. Reverdin, H. Giordani, and G. Caniaux, 2004: Response of the atmospheric boundary layer to a mesoscale oceanic eddy in the northeast Atlantic. *J. Geophys. Res.*, **109**, D18114, https://doi.org/10.1029/2004JD004799.

Brodeau, L., B. Barnier, A.-M. Treguier, T. Penduff, and S. Gulev, 2010: An ERA40-based atmospheric forcing for global ocean circulation models. *Ocean Modell.*, **31**, 88–104, https://doi.org/10.1016/j.ocemod.2009.10.005.

Bye, J. A. T., 1985: Large-scale momentum exchange in the coupled atmosphere–ocean. *Coupled Ocean–Atmosphere Models*, J. C. J. Nihoul, Ed., Elsevier Oceanography Series, Vol. 40, Elsevier, 51–61.

Chassignet, E. P., and D. P. Marshall, 2008: Gulf Stream separation in numerical ocean models. *Ocean Modeling in an Eddying Regime*, *Geophys. Monogr.*, Vol. 177, Amer. Geophys. Union, 39–61.

Chelton, D. B., and S.-P. Xie, 2010: Coupled ocean–atmosphere interaction at oceanic mesoscales. *Oceanography*, **23**, 52–69, https://doi.org/10.5670/oceanog.2010.05.

——, and Coauthors, 2001: Observations of coupling between surface wind stress and sea surface temperature in the eastern tropical Pacific. *J. Climate*, **14**, 1479–1498, https://doi.org/10.1175/1520-0442(2001)014<1479:OOCBSW>2.0.CO;2.

——, M. G. Schlax, and R. M. Samelson, 2007a: Summertime coupling between sea surface temperature and wind stress in the California Current System. *J. Phys. Oceanogr.*, **37**, 495–517, https://doi.org/10.1175/JPO3025.1.

——, ——, ——, and R. A. de Szoeke, 2007b: Global observations of large oceanic eddies. *Geophys. Res. Lett.*, **34**, L15606, https://doi.org/10.1029/2007GL030812.

——, ——, and ——, 2011: Global observations of nonlinear mesoscale eddies. *Prog. Oceanogr.*, **91**, 167–216, https://doi.org/10.1016/j.pocean.2011.01.002.

Chen, F., and J. Dudhia, 2001: Coupling an advanced land surface–hydrology model with the Penn State–NCAR MM5 modeling system. Part I: Model implementation and sensitivity. *Mon. Wea. Rev.*, **129**, 569–585, https://doi.org/10.1175/1520-0493(2001)129<0569:CAALSH>2.0.CO;2.

Chou, M.-D., and M. J. Suarez, 1999: A solar radiation parameterization for atmospheric studies. Tech. Memo. NASA/TM-1999-104606, Vol. 15, 38 pp., https://gmao.gsfc.nasa.gov/pubs/docs/Chou136.pdf.

Colas, F., J. C. McWilliams, X. Capet, and J. Kurian, 2012: Heat balance and eddies in the Peru-Chile Current System. *Climate Dyn.*, **39**, 509–529, https://doi.org/10.1007/s00382-011-1170-6.

Couvelard, X., P. Marchesiello, L. Gourdeau, and J. Lefèvre, 2008: Barotropic zonal jets induced by islands in the southwest Pacific. *J. Phys. Oceanogr.*, **38**, 2185–2204, https://doi.org/10.1175/2008JPO3903.1.

Craig, A., S. Valcke, and L. Coquart, 2017: Development and performance of a new version of the OASIS coupler, OASIS3-MCT_3.0. *Geosci. Model Dev.*, **10**, 3297–3308, https://doi.org/10.5194/gmd-10-3297-2017.

Crétat, J., S. Masson, S. Berthet, G. Samson, P. Terray, J. Dudhia, F. Pinsard, and C. Hourdin, 2016: Control of shortwave radiation parameterization on tropical climate SST-forced simulation. *Climate Dyn.*, **47**, 1807–1826, https://doi.org/10.1007/s00382-015-2934-1.

Dawe, J. T., and L. Thompson, 2006: Effect of ocean surface currents on wind stress, heat flux, and wind power input to the ocean. *Geophys. Res. Lett.*, **33**, L09604, https://doi.org/10.1029/2006GL025784.

Dee, D. P., and Coauthors, 2011: The ERA-Interim reanalysis: Configuration and performance of the data assimilation system. *Quart. J. Roy. Meteor. Soc.*, **137**, 553–597, https://doi.org/10.1002/qj.828.

Dewar, W. K., and G. R. Flierl, 1987: Some effects of the wind on rings. *J. Phys. Oceanogr.*, **17**, 1653–1667, https://doi.org/10.1175/1520-0485(1987)017<1653:SEOTWO>2.0.CO;2.

Dong, C., J. C. McWilliams, Y. Liu, and D. Chen, 2014: Global heat and salt transports by eddy movement. *Nat. Commun.*, **5**, 3294, https://doi.org/10.1038/ncomms4294.

Ducet, N., P.-Y. Le Traon, and G. Reverdin, 2000: Global high-resolution mapping of ocean circulation from TOPEX/Poseidon and ERS-1 and-2. *J. Geophys. Res.*, **105**, 19 477–19 498, https://doi.org/10.1029/2000JC900063.

Duhaut, T. H., and D. N. Straub, 2006: Wind stress dependence on ocean surface velocity: Implications for mechanical energy input to ocean circulation. *J. Phys. Oceanogr.*, **36**, 202–211, https://doi.org/10.1175/JPO2842.1.

Eden, C., and H. Dietze, 2009: Effects of mesoscale eddy/wind interactions on biological new production and eddy kinetic energy. *J. Geophys. Res.*, **114**, C05023, https://doi.org/10.1029/2008JC005129.

Ferrari, R., and C. Wunsch, 2009: Ocean circulation kinetic energy: Reservoirs, sources, and sinks. *Annu. Rev. Fluid. Mech.*, **41**, 253–282, https://doi.org/10.1146/ANNUREV.FLUID.40.111406.102139.

Gaube, P., D. B. Chelton, R. M. Samelson, M. G. Schlax, and L. W. O'Neill, 2015: Satellite observations of mesoscale eddy-induced Ekman pumping. *J. Phys. Oceanogr.*, **45**, 104–132, https://doi.org/10.1175/JPO-D-14-0032.1.

Hallberg, R., 2013: Using a resolution function to regulate parameterizations of oceanic mesoscale eddy effects. *Ocean Modell.*, **72**, 92–103, https://doi.org/10.1016/j.ocemod.2013.08.007.

Hogg, A. M. C., W. K. Dewar, P. Berloff, S. Kravtsov, and D. K. Hutchinson, 2009: The effects of mesoscale ocean–atmosphere coupling on the large-scale ocean circulation. *J. Climate*, **22**, 4066–4082, https://doi.org/10.1175/2009JCLI2629.1.

Hong, S.-Y., and J.-O. J. Lim, 2006: The WRF single-moment 6-class microphysics scheme (WSM6). *J. Korean Meteor. Soc*, **42**, 129–151.

——, Y. Noh, and J. Dudhia, 2006: A new vertical diffusion package with an explicit treatment of entrainment processes. *Mon. Wea. Rev.*, **134**, 2318–2341, https://doi.org/10.1175/MWR3199.1.

Hughes, C. W., and C. Wilson, 2008: Wind work on the geostrophic ocean circulation: An observational study of the effect of small scales in the wind stress. *J. Geophys. Res.*, **113**, C02016, https://doi.org/10.1029/2007JC004371.

Janjić, Z. I., 1994: The step-mountain eta coordinate model: Further developments of the convection, viscous sublayer, and turbulence

closure schemes. *Mon. Wea. Rev.*, **122**, 927–945, https://doi.org/10.1175/1520-0493(1994)122<0927:TSMECM>2.0.CO;2.

Kelly, K. A., S. Dickinson, M. J. McPhaden, and G. C. Johnson, 2001: Ocean currents evident in satellite wind data. *Geophys. Res. Lett.*, **28**, 2469–2472, https://doi.org/10.1029/2000GL012610.

Klein, P., and Coauthors, 2019: Ocean-scale interactions from space. *Earth Space Sci.*, **6**, 795–817, https://doi.org/10.1029/2018EA000492.

Lemarié, F., 2015: Numerical modification of atmospheric models to include the feedback of oceanic currents on air–sea fluxes in ocean–atmosphere coupled models. Tech. Rep. RT-464, INRIA Grenoble-Rhône-Alpes, Laboratoire Jean Kuntzmann, Universite de Grenoble I-Joseph Fourier, INRIA, 6 pp., https://hal.inria.fr/hal-01184711.

Le Traon, P. Y., F. Nadal, and N. Ducet, 1998: An improved mapping method of multisatellite altimeter data. *J. Atmos. Oceanic Technol.*, **15**, 522–534, https://doi.org/10.1175/1520-0426(1998)015<0522:AIMMOM>2.0.CO;2.

Lévy, M., A. Estubier, and G. Madec, 2001: Choice of an advection scheme for biogeochemical models. *Geophys. Res. Lett.*, **28**, 3725–3728, https://doi.org/10.1029/2001GL012947.

——, P. Klein, A. M. Tréguier, D. Iovino, G. Madec, S. Masson, and K. Takahashi, 2010: Modifications of gyre circulation by sub-mesoscale physics. *Ocean Modell.*, **34**, 1–15, https://doi.org/10.1016/j.ocemod.2010.04.001.

Loveday, B. R., J. V. Durgadoo, C. J. Reason, A. Biastoch, and P. Penven, 2014: Decoupling of the Agulhas leakage from the Agulhas Current. *J. Phys. Oceanogr.*, **44**, 1776–1797, https://doi.org/10.1175/JPO-D-13-093.1.

Luo, J.-J., S. Masson, E. Roeckner, G. Madec, and T. Yamagata, 2005: Reducing climatology bias in an ocean–atmosphere CGCM with improved coupling physics. *J. Climate*, **18**, 2344–2360, https://doi.org/10.1175/JCLI3404.1.

Madec, G., 2008: NEMO reference manual, ocean dynamics component: NEMO-OPA. Preliminary version. Note du Pole de modélisation 27, Institut Pierre-Simon Laplace.

Maltrud, M. E., and J. L. McClean, 2005: An eddy resolving global 1/10° ocean simulation. *Ocean Modell.*, **8**, 31–54, https://doi.org/10.1016/j.ocemod.2003.12.001.

McWilliams, J. C., 2008: The nature and consequences of oceanic eddies. *Ocean Modeling in an Eddying Regime*, *Geophys. Monogr.*, Vol. 177, Amer. Geophys. Union, 5–15.

Mellor, G., and A. Blumberg, 2004: Wave breaking and ocean surface layer thermal response. *J. Phys. Oceanogr.*, **34**, 693–698, https://doi.org/10.1175/2517.1.

Mlawer, E. J., S. J. Taubman, P. D. Brown, M. J. Iacono, and S. A. Clough, 1997: Radiative transfer for inhomogeneous atmospheres: RRTM, a validated correlated-k model for the longwave. *J. Geophys. Res.*, **102**, 16 663–16 682, https://doi.org/10.1029/97JD00237.

Nagai, T., N. Gruber, H. Frenzel, Z. Lachkar, J. C. McWilliams, and G.-K. Plattner, 2015: Dominant role of eddies and filaments in the offshore transport of carbon and nutrients in the California Current System. *J. Geophys. Res. Oceans*, **120**, 5318–5341, https://doi.org/10.1002/2015JC010889.

Oerder, V., F. Colas, V. Echevin, S. Masson, C. Hourdin, S. Jullien, G. Madec, and F. Lemarié, 2016: Mesoscale SST–wind stress coupling in the Peru–Chile current system: Which mechanisms drive its seasonal variability? *Climate Dyn.*, **47**, 2309–2330, https://doi.org/10.1007/s00382-015-2965-7.

——, ——, ——, ——, and F. Lemarié, 2018: Impacts of the mesoscale ocean–atmosphere coupling on the Peru-Chile ocean dynamics: The current- induced wind stress modulation. *J. Geophys. Res. Oceans*, **123**, 812–833, https://doi.org/10.1002/2017JC013294.

O'Neill, L. W., S. K. Esbensen, N. Thum, R. M. Samelson, and D. B. Chelton, 2010: Dynamical analysis of the boundary layer and surface wind responses to mesoscale SST perturbations. *J. Climate*, **23**, 559–581, https://doi.org/10.1175/2009JCLI2662.1.

——, D. B. Chelton, and S. K. Esbensen, 2012: Covariability of surface wind and stress responses to sea surface temperature fronts. *J. Climate*, **25**, 5916–5942, https://doi.org/10.1175/JCLI-D-11-00230.1.

Pacanowski, R., 1987: Effect of equatorial currents on surface stress. *J. Phys. Oceanogr.*, **17**, 833–838, https://doi.org/10.1175/1520-0485(1987)017<0833:EOECOS>2.0.CO;2.

Putrasahan, D. A., A. J. Miller, and H. Seo, 2013: Regional coupled ocean–atmosphere downscaling in the southeast Pacific: Impacts on upwelling, mesoscale air–sea fluxes, and ocean eddies. *Ocean Dyn.*, **63**, 463–488, https://doi.org/10.1007/s10236-013-0608-2.

Renault, L., M. J. Molemaker, J. C. McWilliams, A. F. Shchepetkin, F. Lemarié, D. Chelton, S. Illig, and A. Hall, 2016a: Modulation of wind work by oceanic current interaction with the atmosphere. *J. Phys. Oceanogr.*, **46**, 1685–1704, https://doi.org/10.1175/JPO-D-15-0232.1.

——, ——, J. Gula, S. Masson, and J. C. McWilliams, 2016b: Control and stabilization of the Gulf Stream by oceanic current interaction with the atmosphere. *J. Phys. Oceanogr.*, **46**, 3439–3453, https://doi.org/10.1175/JPO-D-16-0115.1

——, J. C. McWilliams, and S. Masson, 2017a: Satellite observations of imprint of oceanic current on wind stress by air–sea coupling. *Sci. Rep.*, **7**, 17747, https://doi.org/10.1038/s41598-017-17939-1.

——, ——, and P. Penven, 2017b: Modulation of the Agulhas Current retroflection and leakage by oceanic current interaction with the atmosphere in coupled simulations. *J. Phys. Oceanogr.*, **47**, 2077–2100, https://doi.org/10.1175/JPO-D-16-0168.1.

——, S. Masson, V. Oerder, S. Jullien, and F. Colas, 2019a: Disentangling the mesoscale ocean–atmosphere interactions. *J. Geophys. Res. Oceans*, **124**, 2164–2178, https://doi.org/10.1029/2018JC014628.

——, P. Marchesiello, S. Masson, and J. C. McWilliams, 2019b: Remarkable control of western boundary currents by eddy killing, a mechanical air–sea coupling process. *Geophys. Res. Lett.*, **46**, 2743–2751, https://doi.org/10.1029/2018GL081211.

——, S. Masson, T. Arsouze, G. Madec, and J. C. McWilliams, 2019c: Recipes for how to force oceanic model dynamics. *J. Adv. Model. Earth Syst.*, https://doi.org/10.1029/2019MS001715, in press.

——, F. Lemarié, and T. Arsouze, 2019d: On the implementation and consequences of the oceanic currents feedback in ocean–atmosphere coupled models. *Ocean Modell.*, **141**, 101423, https://doi.org/10.1016/j.ocemod.2019.101423.

Rimac, A., J.-S. von Storch, C. Eden, and H. Haak, 2013: The influence of high-resolution wind stress field on the power input to near-inertial motions in the ocean. *Geophys. Res. Lett.*, **40**, 4882–4886, https://doi.org/10.1002/grl.50929.

Rooth, C., and L. Xie, 1992: Air–sea boundary layer dynamics in the presence of mesoscale surface currents. *J. Geophys. Res. Oceans*, **97**, 14 431–14 438, https://doi.org/10.1029/92JC01296.

Samson, G., and Coauthors, 2014: The NOW regional coupled model: Application to the tropical Indian Ocean climate and tropical cyclone activity. *J. Adv. Model. Earth Syst.*, **6**, 700–722, https://doi.org/10.1002/2014MS000324.

——, S. Masson, F. Durand, P. Terray, S. Berthet, and S. Jullien, 2017: Roles of land surface albedo and horizontal resolution

on the Indian summer monsoon biases in a coupled ocean–atmosphere tropical-channel model. *Climate Dyn.*, **48**, 1571–1594, https://doi.org/10.1007/s00382-016-3161-0.

Sasaki, H., P. Klein, B. Qiu, and Y. Sasai, 2014: Impact of oceanic-scale interactions on the seasonal modulation of ocean dynamics by the atmosphere. *Nat. Commun.*, **5**, 5636, https://doi.org/10.1038/ncomms6636.

Scott, R. B., and Y. Xu, 2009: An update on the wind power input to the surface geostrophic flow of the World Ocean. *Deep-Sea Res. I*, **56**, 295–304, https://doi.org/10.1016/j.dsr.2008.09.010.

Seo, H., 2017: Distinct influence of air–sea interactions mediated by mesoscale sea surface temperature and surface current in the Arabian Sea. *J. Climate*, **30**, 8061–8080, https://doi.org/10.1175/JCLI-D-16-0834.1.

——, A. J. Miller, and J. R. Norris, 2016: Eddy–wind interaction in the California Current System: Dynamics and impacts. *J. Phys. Oceanogr.*, **46**, 439–459, https://doi.org/10.1175/JPO-D-15-0086.1.

Shchepetkin, A. F., and J. C. McWilliams, 2009: Correction and commentary for ''Ocean forecasting in terrain-following coordinates: Formulation and skill assessment of the regional ocean modeling system'' by Haidvogel et al. *J. Comput. Phys.*, **228**, 8985–9000, https://doi.org/10.1016/j.jcp.2009.09.002.

Skamarock, W. C., 2004: Evaluating mesoscale NWP models using kinetic energy spectra. *Mon. Wea. Rev.*, **132**, 3019–3032, https://doi.org/10.1175/MWR2830.1.

——, and Coauthors, 2008: A description of the Advanced Research WRF version 3. NCAR Tech. Note NCAR/TN-475+STR, 113 pp., https://doi.org/10.5065/D68S4MVH.

Small, R. J., and Coauthors, 2008: Air–sea interaction over ocean fronts and eddies. *Dyn. Atmos. Oceans*, **45**, 274–319, https://doi.org/10.1016/j.dynatmoce.2008.01.001.

Smith, R. D., M. E. Maltrud, F. O. Bryan, and M. W. Hecht, 2000: Numerical simulation of the North Atlantic Ocean at 1/10°. *J. Phys. Ocenogr.*, **30**, 1532–1561, https://doi.org/10.1175/1520-0485(2000)030%3C1532:NSOTNA%3E2.0.CO;2.

Soufflet, Y., P. Marchesiello, F. Lemarié, J. Jouanno, X. Capet, L. Debreu, and R. Benshila, 2016: On effective resolution in ocean models. *Ocean Modell.*, **98**, 36–50, https://doi.org/10.1016/j.ocemod.2015.12.004.

Su, Z., J. Wang, P. Klein, A. F. Thompson, and D. Menemenlis, 2018: Ocean submesoscales as a key component of the global heat budget. *Nat. Commun.*, **9**, 775, https://doi.org/10.1038/s41467-018-02983-w.

Suzuki, N., T. Hara, and P. P. Sullivan, 2014: Impact of dominant breaking waves on air–sea momentum exchange and boundary layer turbulence at high winds. *J. Phys. Oceanogr.*, **44**, 1195–1212, https://doi.org/10.1175/JPO-D-13-0146.1.

——, B. Fox-Kemper, P. E. Hamlington, and L. P. Van Roekel, 2016: Surface waves affect frontogenesis. *J. Geophys. Res. Oceans*, **121**, 3597–3624, https://doi.org/10.1002/2015JC011563.

Villas Bôas, A., O. T. Sato, A. Chaigneau, and G. P. Castelão, 2015: The signature of mesoscale eddies on the air–sea turbulent heat fluxes in the South Atlantic Ocean. *Geophys. Res. Lett.*, **42**, 1856–1862, https://doi.org/10.1002/2015GL063105.

Xu, C., X. Zhai, and X.-D. Shang, 2016: Work done by atmospheric winds on mesoscale ocean eddies. *Geophys. Res. Lett.*, **43**, 12 174–12 180, https://doi.org/10.1002/2016GL071275.

Xu, Y., and R. B. Scott, 2008: Subtleties in forcing eddy resolving ocean models with satellite wind data. *Ocean Modell.*, **20**, 240–251, https://doi.org/10.1016/j.ocemod.2007.09.003.

Zhai, X., and R. J. Greatbatch, 2007: Wind work in a model of the northwest Atlantic Ocean. *Geophys. Res. Lett.*, **34**, L04606, https://doi.org/10.1029/2006GL028907.

——, H. L. Johnson, and D. P. Marshall, 2010: Significant sink of ocean-eddy energy near western boundaries. *Nat. Geosci.*, **3**, 608–612, https://doi.org/10.1038/ngeo943.

——, ——, ——, and C. Wunsch, 2012: On the wind power input to the ocean general circulation. *J. Phys. Oceanogr.*, **42**, 1357–1365, https://doi.org/10.1175/JPO-D-12-09.1.